

<b>REPORT DOCUMENTATION PAGE</b>				Form Approved OMB No. 0704-0188	
Public reporting burden for this collection of information is estimated to average 1 hour per response, including the time for reviewing instructions, searching existing data sources, gathering and maintaining the data needed, and completing and reviewing the collection of information. Send comments regarding this burden estimate or any other aspect of this collection of information, including suggestions for reducing the burden, to Department of Defense, Washington Headquarters Services, Directorate for Information Operations and Reports (0704-0188), 1215 Jefferson Davis Highway, Suite 1204, Arlington, VA 22202-4302. Respondents should be aware that notwithstanding any other provision of law, no person shall be subject to any penalty for failing to comply with a collection of information if it does not display a currently valid OMB control number. <b>PLEASE DO NOT RETURN YOUR FORM TO THE ABOVE ADDRESS.</b>					
<b>1. REPORT DATE (DD-MM-YYYY)</b> 17-01-2006		<b>2. REPORT TYPE</b> Final Report		<b>3. DATES COVERED (From – To)</b> 1 January 2004 - 15 October 05	
<b>4. TITLE AND SUBTITLE</b>  Experimental Investigations And Numerical Modeling Of Optical Phase Modulation By Dual-Frequency Nematic Liquid Crystals				<b>5a. CONTRACT NUMBER</b> FA8655-03-D-0001, Delivery Order 0015	
				<b>5b. GRANT NUMBER</b>	
				<b>5c. PROGRAM ELEMENT NUMBER</b>	
<b>6. AUTHOR(S)</b>  Dr. Mikhail Ivanovich Barnik				<b>5d. PROJECT NUMBER</b>	
				<b>5d. TASK NUMBER</b>	
				<b>5e. WORK UNIT NUMBER</b>	
<b>7. PERFORMING ORGANIZATION NAME(S) AND ADDRESS(ES)</b> Shubnikov Institute of Crystallography Leninsky prosp. 59 Moscow 117333 Russia				<b>8. PERFORMING ORGANIZATION REPORT NUMBER</b>  N/A	
<b>9. SPONSORING/MONITORING AGENCY NAME(S) AND ADDRESS(ES)</b>  EOARD PSC 821 BOX 14 FPO 09421-0014				<b>10. SPONSOR/MONITOR'S ACRONYM(S)</b>	
				<b>11. SPONSOR/MONITOR'S REPORT NUMBER(S)</b> EOARD Task 03-9008	
<b>12. DISTRIBUTION/AVAILABILITY STATEMENT</b>  Approved for public release; distribution is unlimited.					
<b>13. SUPPLEMENTARY NOTES</b>					
<b>14. ABSTRACT</b>  This report results from a contract tasking Shubnikov Institute of Crystallography as follows: The contractor will investigate electro-optical effects and physical properties of liquid crystal materials (LCM) to improve spatial phase modulation for steering light. The primary goal is to develop liquid crystal (LC) based techniques for fast phase modulation. As noted in the technical proposal, the ultimate objective is to achieve the following performance characteristics of optical phase modulators: 1) 100% phase modulation not less than 2pi radian in the visible and near IR spectral band; 2) the time of 2pi-phase retardation switching is less than 1-2 ms (at the switching repetition rate higher than 250 Hz) 3) LC-material transparency in the spectral band of 800-1550 nm; 4) driving voltage less than ±50 V; 5) wide operating temperature range (including the range below room temperatures).					
<b>15. SUBJECT TERMS</b> EOARD, Liquid Crystals, Spatial light modulators					
<b>16. SECURITY CLASSIFICATION OF:</b>			<b>17. LIMITATION OF ABSTRACT</b> UL	<b>18. NUMBER OF PAGES</b>  22	<b>19a. NAME OF RESPONSIBLE PERSON</b> PAUL LOSIEWICZ, Ph. D.
<b>a. REPORT</b> UNCLAS	<b>b. ABSTRACT</b> UNCLAS	<b>c. THIS PAGE</b> UNCLAS			<b>19b. TELEPHONE NUMBER</b> (Include area code) +44 20 7514 4474

# Experimental investigations and numerical modeling of optical phase modulation by dual-frequency nematic liquid crystals

Mikhail I. Barnik, Vladimir V. Lazarev, Serguei P. Palto

Shubnikov Institute of Crystallography of Russian Academy of Sciences, Leninsky pr.59,  
119333 Moscow, Russia

Experimental study and numerical simulations of optical phase modulators based on nematic liquid crystals characterized by frequency sign inversion of the dielectric anisotropy has been performed. The received results point out an extreme role of back-flow effects and electro-hydrodynamic instability, which make restrictions for creating high-speed phase modulators.

## 1. Introduction

For a long time nematic liquid crystals (NLCs) are used in adaptive optics for wavefront shaping and control (see [1-14], for instance). The optical phase modulation realized in such devices is due to optical retardation, which appears as a result of field-driven NLC director (optical axis) reorientation. For instance, the planar LC director field distribution characterized by in-plane orientation of the optical axis can be switched by electric field to the homeotropic director field distribution, when the optical axis becomes normal to the LC layer. In case of positive dielectric anisotropy of the LC ( $\epsilon_a = \epsilon_{\parallel} - \epsilon_{\perp} > 0$ , where  $\epsilon_{\parallel}$  and  $\epsilon_{\perp}$  are the dielectric permittivity along and perpendicular to the LC director respectively) the latter is possible by using an electric field applied along the LC layer normal. In this example the switching speed to the homeotropic state can be raised by increasing the electric field strength. For typical LC parameters and reasonable strength of the electric field of about 10 V/ $\mu\text{m}$  the field-on switching time can be as low as 100 $\mu\text{s}$ . However, the back relaxation to the ground planar state is still defined by viscous-elastic properties of LC material, so the relaxation speed is restricted. Even for low viscosity materials (with the rotational viscosity  $\gamma \sim 0.05$  Pa s, and elastic coefficients  $K_{1,2,3} \sim 10$  pN) at LC layer thickness of 5 $\mu\text{m}$  the relaxation time is of about 15ms. Quite similar situation, but with opposite direction of the optical axis driving, takes place if the initial LC director field distribution is homeotropic, but the LC has the negative dielectric anisotropy ( $\epsilon_a < 0$ ). Thus, one of the main drawbacks of the LC-based modulators that make restrictions for the modulation speed, is due to existence of the free viscous-elastic relaxation. Fortunately, there are liquid crystal materials, which allow excluding the free relaxation stages from the modulation process. These are so-called dual-frequency liquid crystals (2f-LCM) [15-20], which show

inversion of the dielectric anisotropy sign at some frequency, which is typically located in sound-frequency band. Using the dual-frequency driving one can realize field-driven reorientation of the LC optical axis to both homeotropic and planar states. There are many examples of 2f-LCMs applications for the optical phase modulation [21-26]. Due to possibility of excluding the free relaxation stages from the modulation process it is believed that using the 2f-LCMs will allow creating very fast phase modulators [27,28].

Recently [29] we have studied the dynamical properties of 2f-LCMs phase modulators. The stable switching to any desired state characterized by phase retardation within the range from 0 to  $2\pi$  has been achieved for times less than 1 ms. This switching was realized for layers of thicknesses larger than 7  $\mu\text{m}$ . For example, to obtain such phase modulation parameters for a layer of the 2f-LCM as thick as 8  $\mu\text{m}$ , it is sufficient to use the low-frequency (2 kHz) driving voltage of 50 V and high-frequency voltage (35 kHz) of 30 V. We have also assumed that high-frequency driving induces extra back-flow coupling, which then provokes experimentally observed hydrodynamic instabilities restricting high-speed performance of the modulators.

In this paper we clarify reasons for restrictions of high-speed modulation in more details. In addition to the experimental study we show the results of the numerical simulations of the 2f-LCMs switching. These numerical simulations agree with the experimental observations and give explicit confirmation for the principal role of back-flow hydrodynamic coupling, which makes restriction in creating high-speed optical phase modulators. The simulation results point out the principal LC parameters to be improved in order to get highest performance of the 2f-LCM phase modulators.

## 2. Experiment and Results

Experimental data were received on a specially developed 2f-LCM mixture called AP-99-1. This mixture is characterized by following physical parameters at room temperature ( $T = 21^\circ\text{C}$ ):  $\varepsilon_a$  (1 kHz) = 2.4,  $\varepsilon_a$  (40 kHz) = -2.6,  $f_i = 9$  kHz, optical anisotropy  $\Delta n = n_{\parallel} - n_{\perp} = 0.25$  ( $n_{\parallel} = n_e$  and  $n_{\perp} = n_o$  are refractive indices along and perpendicular to the LC director, respectively), splay and bend elastic constant are equal  $K_1 = 9.7$  pN and  $K_3 = 16.5$  pN, respectively. The temperatures of phase transitions are found to be as follows: from nematic to smectic  $T_{\text{NS}} = -7^\circ\text{C}$  and from isotropic to nematic  $T_{\text{I-N}} = 74^\circ\text{C}$  at cooling and from nematic to isotropic  $T_{\text{N-I}} = 78^\circ\text{C}$  at heating.

The electro-optical investigations were made on cells with planarly aligned LC layers. The LC alignment was due to the boundary conditions providing the director pretilt angles of the same sign at opposite surfaces. These boundary conditions were controlled by rubbing of the

polyimide alignment layers in opposite ("antiparallel") directions that gives a pretilt angle of  $|\Theta| \sim 3^\circ\text{-}4^\circ$  [30]. The cell of such a director arrangement is referred below as a cell of homogeneous alignment, or "0-aligned" cell. For the 0-aligned cells the director field is uniform accrosst the thickness of LC layer. The cells were placed between crossed polarizers. The He-Ne laser was used as a light source. The dual-frequency modulated pulse packets consisting of a sequence of low frequency (1 kHz) square-waveform pulses and high frequency (35 kHz) sinusoidal waves were used for driving. The details of the method for measuring the optical phase modulation properties were described in [29].

Two geometries distinguished by LC director orientation (i.e. rubbing direction  $R$  of alignment layers) with respect to the direction  $P$  defining the axis of the input polarizer were used in our experiments: i) "RP<sub>45</sub>", when the rubbing direction turned at an angle of  $45^\circ$ ; (ii)"RP<sub>0</sub>", when the rubbing direction is at an angle of  $0^\circ$ . In all the measurements the input and output polarizers were crossed. For RP<sub>45</sub> geometry, in case of non-twisted LC director field distribution, the intensity  $I$  of the outgoing light and the phase retardation  $\Delta\Phi$  are related as:

$$I = I_0 \sin^2\left(\frac{\Delta\Phi}{2}\right), \quad (1)$$

where  $I_0$  is approximately (neglecting reflections and non-ideality of the polarizers) half of the intensity of the incoming nonpolarized light and

$$\Delta\Phi = \frac{2\pi}{\lambda} d \Delta n, \quad (2)$$

where  $\lambda$  is wavelength and  $d$  is LC layer thickness. Note right here that for RP<sub>0</sub> geometry the electro-optical response can be non-zero only if a twist deformation appears in the director field distribution.

Fig. 1 demonstrates the electro-optical response for two different cells with LC layer thickness of  $7.6\ \mu\text{m}$  and  $10\ \mu\text{m}$ . For these thicknesses values the field-off states correspond to phase retardations of about  $6\pi$  and  $8\pi$ , respectively. Maximum values of transmission ( $T=1$ ) are achieved at odd multiple of  $\pi$  phase retardations. The driving waveform is shown at the bottom in the Fig.1. Both low and high frequency driving waveforms are of 1 ms in duration.

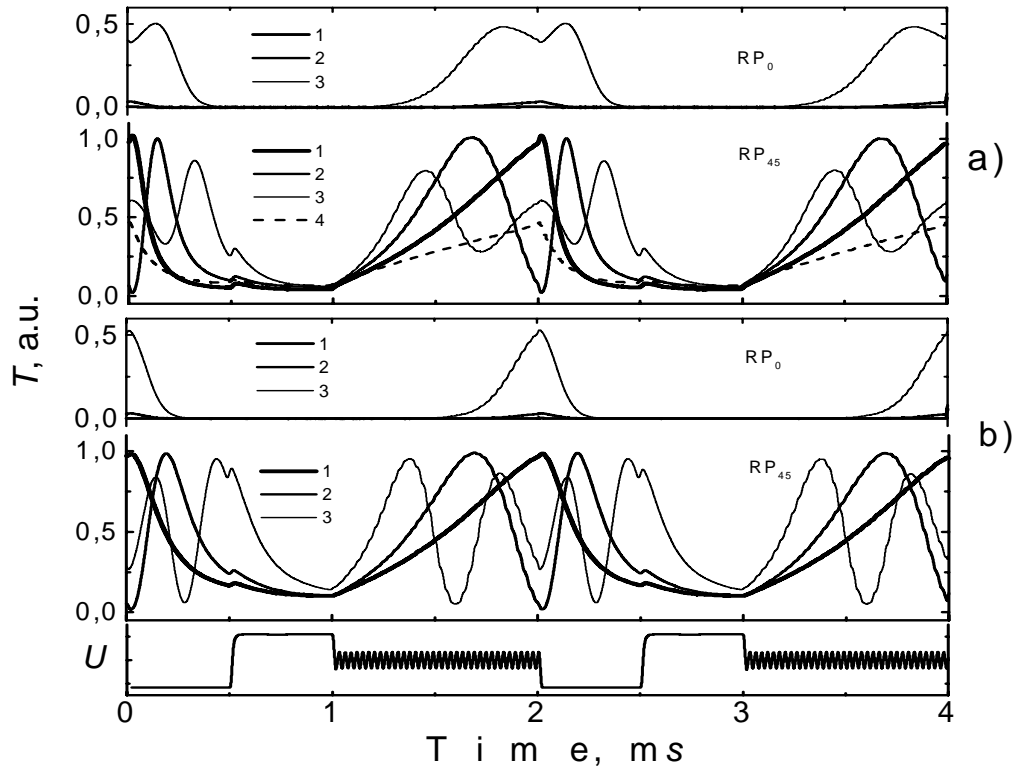


Fig. 1. Electro-optical response measured for the 0-aligned AP-99-1 layers in  $RP_{45}$  and  $RP_0$  geometries at  $U_{LF} = 50V$  and  $T = 22^\circ C$ ): a)  $d = 7.6 \mu m$ , curve 1-4 are for  $U_{HF} = 22, 30, 40$  and  $0$  V, respectively; b)  $d = 10 \mu m$ , curve 1-3 are for  $U_{HF} = 30, 38$  and  $51$  V, respectively. The lower trace represents the applied voltage waveform.

As it is seen in Fig. 1, the low frequency driving waveform of about 50 V in amplitude is sufficient to achieve almost homeotropic director field distribution that provides the phase retardation  $\Delta\Phi$  to be very close to zero. In the dynamic mode the phase retardation of  $2\pi$  not always can be achieved, despite the two layers are capable to provide a phase retardation of  $6\pi$  and  $8\pi$  respectively in the quasi-static regime. The latter is proved by absence of 100% intensity modulation in the electrooptical response. The amplitudes of high frequency voltage  $U_{HF}$  are 30 and 38 V for LC layer thickness of 7.6  $\mu m$  and 10  $\mu m$  respectively. At first glance with increasing the high frequency amplitude  $U_{HF}$  at a fixed low frequency voltage  $U_{LF}$  the LC director field distribution after fixed time interval should become closer to the planar state, and the phase retardation have to be increased. However, one can see that after exceeding some certain value of  $U_{HF}$ , the maximum transmission in  $RP_{45}$  geometry begins to fall down and 100% intensity modulation is not reached. At the same instant, the step-wise growth of the transmission appears in  $RP_0$  geometry. A non-zero transmission in  $RP_0$  geometry can only be explained if LC director field is subjected to the twist deformation. By additional experiments we have established that the observed behavior takes place just before the electrohydrodynamic (EHD) instability, which appears at larger high-frequency fields. The EHD is a result of complex

hydrodynamics developed in LC layer, when high frequency driving voltage exceeds a certain threshold value. At voltages higher than threshold values the EHD instability is characterized by appearance of periodic distortions of LC texture. In  $RP_0$  geometries the EHD instability looks like striped (black-bright) domains oriented along the rubbing direction. At further growth of  $U_{HF}$ , regular hydrodynamic flows become turbulent and accompanied by strong light scattering [29].

The experimental study was performed for LC layers of thickness varied in a range of 2.5-12.5  $\mu\text{m}$ . In Fig. 2 we summarize the experimental results on thickness dependencies of the high-frequency driving voltage  $U_{HF}$  for: i) EHD instability appearance (curve 1); for stable  $2\pi$ -modulation (curve 2); iii) for stable  $\pi$ -modulation (curve 3). The low frequency voltage  $U_{LF}$  in all these experiments is maintained at a constant value of 50 V. The plot area above the curve 1 corresponds to EHD instability. Due to EHD instability restrictions the fast (500 Hz) stable  $2\pi$  phase modulation can only be realized if LC layer thickness is larger than 7  $\mu\text{m}$ . For thinner layers within a thickness range from 3  $\mu\text{m}$  to 6  $\mu\text{m}$  a maximum phase modulation of  $\pi$  can only be achieved (see Fig. 2, curve 3).

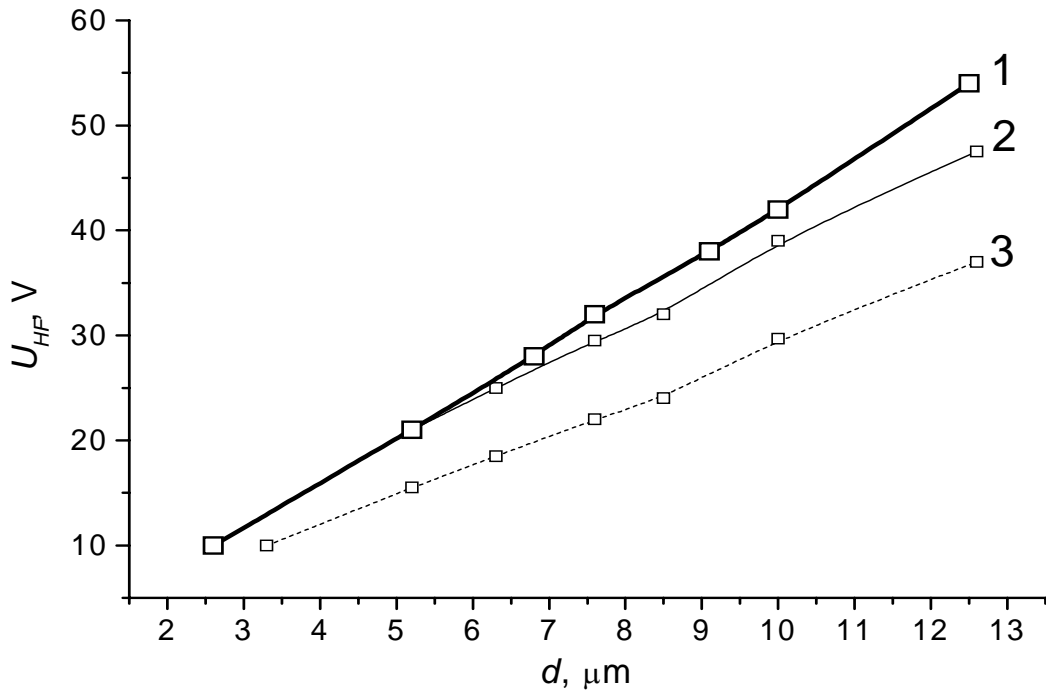


Fig. 2. Thickness dependence of high frequency (35 kHz) voltage  $U_{HF}$  at which a dynamic phase retardation change of  $\pi$  (3) and  $2\pi$  (2) is still achieved (100% light modulation efficiency is observed). The curve 1 shows dependence of the threshold voltage of dynamic phase modulation breakdown. The data are for the 0-aligned AP-99-1 layers at  $T = 22^\circ\text{C}$

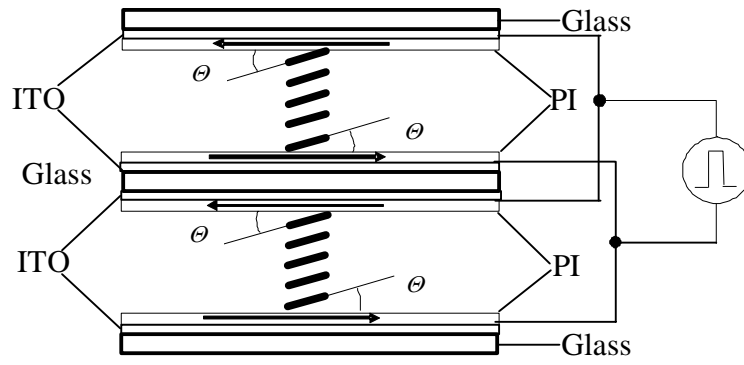


Fig. 3. A sketch of the double-layer liquid crystal cell and its connection to the net source. The arrows show the directions of rubbing.

Double-layer LC cells can be used to expand the dynamic range of fast optical phase modulation. In this case the same speed at equivalent modulation is achieved at lower values of the high-frequency voltage, when LC is not subjected to EHD instability. A double-layer cell design and its electric connection to the net source are schematically shown in Fig.3. The cell assembly consists of three stacked glass plates with two gaps between them, which are filled by AP-99-1 LC material. The inner surfaces of the two outer plates and the both surfaces of the middle plate have ITO electrodes, coated with alignment polyimide layers, which are rubbed in the directions designated by arrows in the Fig. 3 to provide planar homogeneous LC alignment.

Fig. 4 shows oscillogramms of electro-optic response for the double-layer cells with different LC layers thickness of 6.8 and 7.3  $\mu\text{m}$ , when the electric circuit providing the parallel connection of layers to the voltage source is used (see Fig. 3). Thus, each layer is driven by the same periodic pulse sequence consisting of the low frequency (1  $\text{kHz}$ ) square-waveform at fixed voltage values  $U_{LF} = 50 \text{ V}$ , and the high frequency 35  $\text{kHz}$  sinusoidal waveform at different values  $U_{HF}$ . Firstly, it is necessary to note that maximum transmission of the double-layer cell in case of  $\text{RP}_{45}$  geometry is approximately twice less than that of the single-layer cell (compare with Fig. 1). This is an effect of increasing from 2 to 4 in the number of ITO electrodes, which absorb and reflect some portions of light (transmission coefficient of a single plate with ITO electrode we used is as large as 0.8). The problem of reduced transmission can be resolved to a great extent by known technological ways: using a less absorbing electrode coating, antireflective coverings and so forth. Another feature of the double-layer cell operation is an increased light leakage in the dark state, when the LC director is driven to the homeotropic state. The latter is due to increased number of LC interfacial layers, which are never reoriented to the ideally homeotropic states because of the strong surface anchoring. This light leakage in the dark state can be considerably reduced by increasing the voltage amplitude of low frequency driving

and/or by weakening the anchoring conditions at the interfaces. Another way is using of external retarder films to provide optical compensation of these quasi-homeotropic interfacial LC layers.

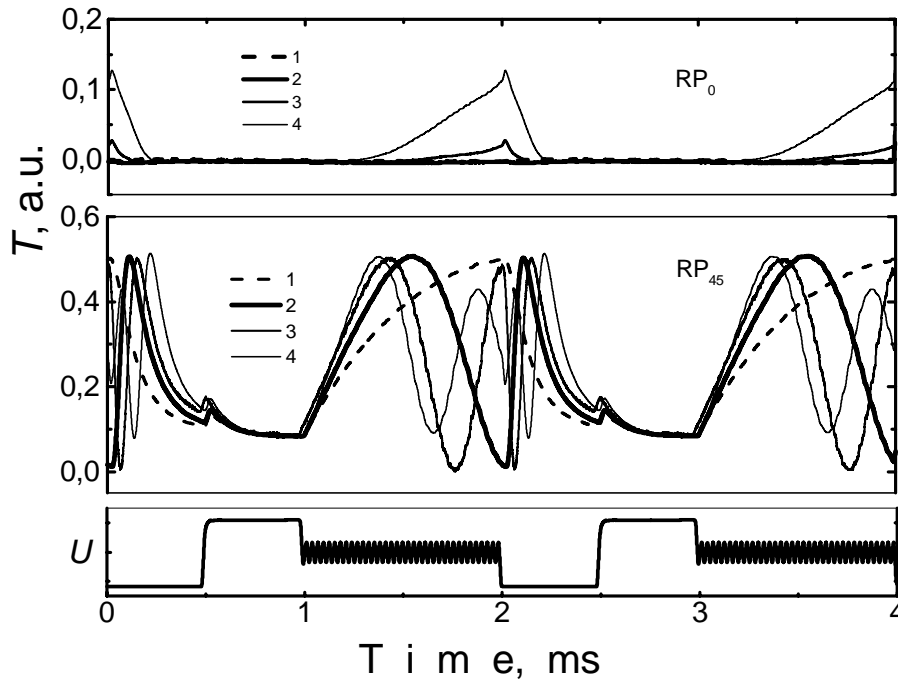


Fig. 4. Electro-optical response of the 0-aligned AP-99-1 layers in a double layer (6.8 and 7.3  $\mu\text{m}$ ) cell measured in  $\text{RP}_{45}$  and  $\text{RP}_0$  geometries at  $U_{LF} = 50\text{V}$  ( $T = 22^\circ\text{C}$ ): curve 1-4 are for  $U_{HF} = 0, 22, 28$  and  $32\text{ V}$ , respectively

The basic positive result obtained on the double-layer cell is the following. It is clearly seen from the Fig. 4 that the equal in value, say  $2\pi$ , phase retardation change for the double-layer cells and ordinary single-layer cells is reached at different high frequency voltages. The voltage is by a factor of  $\sim 1.4$  less for the double-layer design compared to single-layer one. In particular case the high frequency voltage magnitudes are  $22\text{ V}$  for the double-layer design and  $\sim 32\text{ V}$  for the single-layer cell. Owing to such a marked reduction of driving voltage, it is possible to realize stable switching of phase retardation even in the range from  $0$  to  $3\pi$ , while for the single-layer cell, at the same voltages, the undistorted fast phase retardation switching is hardly realized in the dynamic range from  $0$  to  $2\pi$ .



### 3. Numerical simulation

We made comprehensive numerical analysis of the light polarization state dynamics for the two virtual systems to clarify reasons for restrictions of speed and value of phase modulators in case of using the dual-frequency LC materials. For the first type of the system the hydrodynamic coupling was suppressed, i.e. the dynamics of the LC director field deformation has been calculated only on account of the rotational viscosity, while in the second case the set of dynamic equations is extended to take into account the hydrodynamics. In the latter case the viscous properties are described by five independent Leslie coefficients.

The simulations have been performed using LCD TDK 2.0 software package, which was created by one of participants (P.S.P.) of this project for solving different problems in field of electro-optical properties of LC devices.

#### 3.1. Simulated Set-Up

The scheme of the simulated set-up is shown in Fig .5. The LC cell is placed between two crossed polarizers with the transmission axes oriented at an angle of 45 degrees with respect to the  $x$  axis of the laboratory frame  $xyz$ . The polarizers are assumed to be of high optical performance. In calculations the polarizers are simulated by plates of thickness of  $2\text{ }\mu\text{m}$  made of material providing the dichroic ratio of  $k_{\parallel}/k_{\perp}=100$  ( $k_{\parallel}=3\text{ }\mu\text{m}^{-1}$ ,  $k_{\perp}=0.03\text{ }\mu\text{m}^{-1}$ ).

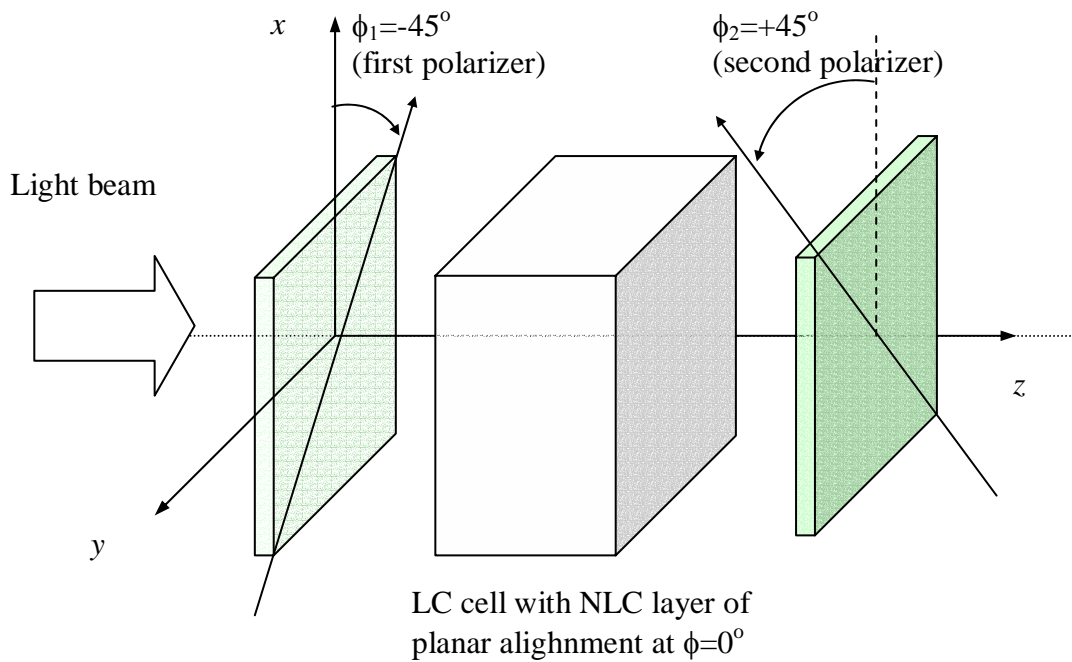


Fig. 5. Scheme of simulated electro-optical set-up.

The LC layers of thickness of 5  $\mu\text{m}$  are simulated, and they are assumed to be homogeneously aligned, so at the layer boundaries the LC director has almost planar orientation along the  $x$  axis (small pretilt angle of 4 degrees typically realized in practice is defined in calculations). To study the stability of the director field with respect to the hydrodynamics we have also introduced small azimuthal angular difference of one degree in easy axes orientations at the LC layer boundaries. This difference typically exists in experimental cells due to technological inaccuracies (rubbing and cell assembling procedure). Some of LC parameters are fixed in simulations, while the others are variable. Around the fixed quantities are the elastic constants ( $K_1=10$  pN,  $K_2=5$  pN,  $K_3=15$  pN), rotational viscosity  $\gamma=0.5$  Pa s, optical anisotropy  $\Delta n=0.2$ , low-frequency dielectric anisotropy  $\varepsilon_a=+5$ , high-frequency dielectric anisotropy  $\varepsilon_a=-4$ . The used values are close to ones of typical dual-frequency materials used in experimental part of this work, but they do not match them exactly. The latter is not of principal significance for the general features of the discussed problem.

### 3.2 Basic equations for calculations of the dynamics of the director field under external electric field

We are considering an LC layer, which is homogeneously aligned in the  $xy$  plane directions of the laboratory frame system. The external electric field can be applied in the  $z$ -direction that is perpendicular to the LC layer plane. Thus the inhomogeneous director field distribution takes place only along the  $z$ -direction, and the mathematical problem is one-dimensional.

#### 3.2.1. Equations in case of neglecting the hydrodynamic coupling

In cases we neglect the hydrodynamic coupling the Euler-Lagrange formalism results in the following set of equations describing the dynamics of the LC director field distribution  $\vec{n}(z,t) = (n_x(z,t), n_y(z,t), n_z(z,t))$ :

$$\gamma \frac{\partial n_x}{\partial t} = \lambda n_x - \frac{\partial F}{\partial n_x} + \frac{d}{dz} \frac{\partial F}{\partial n_x}, \quad (3)$$

$$\gamma \frac{\partial n_y}{\partial t} = \lambda n_y - \frac{\partial F}{\partial n_y} + \frac{d}{dz} \frac{\partial F}{\partial n_y}, \quad (4)$$

$$\gamma \frac{\partial n_z}{\partial t} = \lambda n_z - \frac{\partial F}{\partial n_z} + \frac{d}{dz} \frac{\partial F}{\partial n_z}, \quad (5)$$

where  $\gamma$  is the rotational viscosity,  $\lambda$  is Lagrange multiplier and  $n_{x,y,z}' \equiv \frac{\partial}{\partial z} n_{x,y,z}$ . Typical values of the rotational viscosity for the dual-frequency materials are in a range of 0.4 – 0.7 Pa s. In the case of nonchiral LCs the free energy density  $F$  is expressed in terms of both elastic and electric field energy densities as follows:

$$F = \frac{1}{2} \left\{ K_{11} n_z'^2 + K_{22} (n_y n_x' - n_x n_y')^2 + K_{33} [n_z^2 (n_y'^2 + n_x'^2) + (n_x n_x' + n_y n_y')^2] \right\} + \frac{1}{2} \frac{D_z^2}{\epsilon_{\perp} \left( 1 + \frac{\epsilon_{\parallel} - \epsilon_{\perp}}{\epsilon_{\perp}} n_z^2 \right)}, \quad (6)$$

where  $K_{ii}$  are the elastic modules responsible for different types of the deformations. The electric field contribution is expressed in terms of electric displacement  $D_z$ , which remains independent of  $z$  due to negligible conductivity of the LC layer. The relationship between the electric displacement and applied voltage  $V$  is:

$$V = \int_0^d E(z) dz = \frac{D_z}{\epsilon_{\perp}} \int_0^d \frac{1}{\left( 1 + \frac{\epsilon_{\parallel} - \epsilon_{\perp}}{\epsilon_{\perp}} n_z^2 \right)} dz. \quad (7)$$

For dual-frequency materials the dielectric anisotropy  $\epsilon_a$  is frequency dependent. It is positive at low-frequencies (typically less than a few kHz) and negative if the high-frequency field is applied (typically  $f > 5-10$  kHz).

### 3.2.2. Equations in case of the hydrodynamic coupling is taken into account

On account of Leslie theory [31] the total set of equations becomes

$$\frac{\partial}{\partial z} \left[ \alpha_2 n_z \frac{\partial n_x}{\partial t} + \alpha_3 n_x \frac{\partial n_z}{\partial t} + \frac{1}{2} \alpha_3 n_x n_y V_y' + \frac{1}{2} (2\alpha_1 n_x^2 n_z^2 - \alpha_2 n_z^2 + \alpha_3 n_x^2 + \alpha_4 + \alpha_5 n_z^2 + \alpha_6 n_x^2) V_x' \right] = 0, \quad (8)$$

$$\frac{\partial}{\partial z} \left[ \alpha_2 n_z \frac{\partial n_y}{\partial t} + \alpha_3 n_y \frac{\partial n_z}{\partial t} + \frac{1}{2} \alpha_3 n_x n_y V_x' + \frac{1}{2} (2\alpha_1 n_y^2 n_z^2 - \alpha_2 n_z^2 + \alpha_3 n_y^2 + \alpha_4 + \alpha_5 n_z^2 + \alpha_6 n_y^2) V_y' \right] = 0, \quad (9)$$

$$\gamma \frac{\partial n_x}{\partial t} = \lambda n_x - \frac{\partial F}{\partial n_x} + \frac{d}{dz} \frac{\partial F}{\partial n_x}, -\alpha_2 n_z V_x', \quad (10)$$

$$\gamma \frac{\partial n_y}{\partial t} = \lambda n_y - \frac{\partial F}{\partial n_y} + \frac{d}{dz} \frac{\partial F}{\partial n_y}, -\alpha_2 n_z V_y', \quad (11)$$

$$\gamma \frac{\partial n_z}{\partial t} = \lambda n_z - \frac{\partial F}{\partial n_z} + \frac{d}{dz} \frac{\partial F}{\partial n_z}, -\alpha_3 n_x V_x' - \alpha_3 n_y V_y', \quad (12)$$

where  $V_{x,y}$  are the velocity components of the hydrodynamic flow and  $\alpha_i$  - the viscosity coefficients, which are also known as Leslie coefficients. The rotational viscosity is also expressed in terms of Leslie coefficients as  $\gamma = \alpha_3 - \alpha_2$ . According to theoretical and experimental studies the values of  $\alpha_1$  and  $\alpha_3$  are much less than the values of the other coefficients, so they are neglected in current simulations.

### 3.3. Basics of the approach for the optical calculations

The optical calculations are based on exact solution of Maxwell equations for one-dimensionally inhomogeneous anisotropic media. The Berreman 4×4 matrix approach [32] with numerical algorithm described in [33] is used to calculate the transmission, reflection and corresponding light polarization states for the system shown in Fig. 5. In case of the light polarization state calculations the second (output) polarizer is not taken into account.

If the media is homogeneous in the  $xy$ -plane the system of six Maxwell equations is reduced to the system of only four independent equations, and the wave propagating equations can be written in terms of the first order differential equations as

$$\frac{\partial}{\partial z} \Psi = \frac{i\omega}{c} \Delta \cdot \Psi, \quad (13)$$

where the components of matrix  $\Delta$  are expressed in terms of dielectric tensor components [32, 33], and the electromagnetic field column  $\Psi$  is defined through the electric ( $E_{x,y}$ ) and magnetic field ( $H_{x,y}$ ) components as follows:

$$\Psi = \begin{pmatrix} E_x \\ H_y \\ E_y \\ -H_x \end{pmatrix}. \quad (14)$$

It is evident that the solution of (13) for an homogeneous optically anisotropic slab of thickness  $h$  is

$$\Psi(h) = \exp(i\omega h\Delta/c)\Psi(0) \equiv P(h)\Psi(0), \quad (15)$$

where  $\Psi(0)$  and  $\Psi(h)$  are the electromagnetic field columns at the input ( $z=0$ ) and output ( $z=h$ ) of the slab respectively. Actually, the problem is reduced to calculation of the exponent of the matrix  $\Delta$  and finding the matrix  $P(h)$ . In case of multilayered optical systems one needs to calculate the product of matrices  $P_i(h_i)$  of the individual layers the system consists of. Similarly, in the case of the inhomogeneous LC layer the problem is solved by space discretization (sampling) of the whole layer thickness along the  $z$ -axis and finding the product of the corresponding matrices. The details on how to efficiently evaluate the field, transmission and reflection are described in [33].

The analysis of the polarization state is performed in a frame of the Stokes vector concept using Poincaré sphere presentation after the output field is calculated. By expressing the output electric field components in form

$$\begin{aligned} E_x &= A_x \cos(\omega t - kz + \delta_x) \\ E_y &= A_y \cos(\omega t - kz + \delta_y), \end{aligned} \quad (16)$$

the Stokes vector components are defined as follows:

$$S = \begin{pmatrix} S_0 \\ S_1 \\ S_2 \\ S_3 \end{pmatrix} = \begin{pmatrix} A_x^2 + A_y^2 \\ A_x^2 - A_y^2 \\ 2A_x A_y \cos \delta \\ 2A_x A_y \sin \delta \end{pmatrix}, \quad (17)$$

where  $\delta = \delta_y - \delta_x$ . It can easily be checked that

$$S_0^2 = S_1^2 + S_2^2 + S_3^2, \quad (18)$$

so all the light polarization states belong to the sphere surface of radius  $S_0$  (it is called Poincaré sphere), which is just represent the intensity of the polarized light. The points on the equator of the Poincaré sphere represent all the linear polarizations, while the other ones are for elliptical polarizations, which become circular at the poles. According to the classic definition, the circular polarization is right handed if the clockwise time revolution of the field vector takes place for an observer the photon arrives to. If this convention is used then the right-handed circular state is located at the north pole of the Poincaré sphere. For the set-up shown in Fig. 5 the light

polarization states should belong to the  $90^\circ$  meridian, and the points where this meridian is crossed with the equator correspond to the linear polarization states, which are either completely blocked or transmitted by the output polarizer.

### 3.3 Results of the simulations

#### 3.3.1 Transmission response and dynamics of the polarization state in absence of hydrodynamic flows

The results of numerical simulations are shown in Fig. 6 and Fig. 7. The Fig. 6 shows the transmission coefficient change under low frequency ( $t= 0 - 2$  ms) and high frequency ( $t=2 - 4$  ms) driving with an external voltage of 50 V (effective value) at  $\lambda=550\text{nm}$ . The total phase retardation change is somewhat less than  $4\pi$ . The response to the high frequency pulse is slower compared to the low frequency one for two reasons. Firstly, this is due to a lower value of the high frequency anisotropy ( $\varepsilon_a = -4$ ) compared to the low frequency value ( $\varepsilon_a = +5$ ). Secondly, the director field distribution at the moment the high frequency pulse applied is very close to the homeotropic state and, thus, very low torque appears at the beginning of high frequency pulse, so significant delay of 500 microseconds is well visible during interval from  $t=2$  to  $t=2.5$  ms.

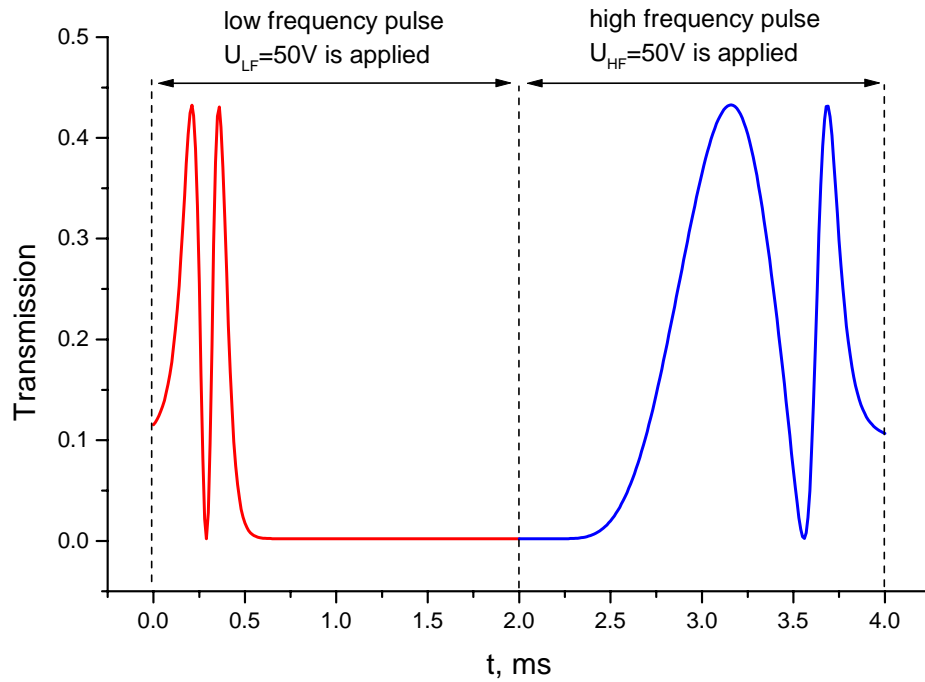


Fig. 6. Dynamics of optical transmission response in case of dual-frequency driving, when the hydrodynamic coupling is neglected

It is very important that the director reorientation is stable. The molecular reorientation under the electric field appears just in the  $xz$  plane that results in the light polarization states



single package dual frequency driving; ( $U_{LF}=U_{HF}=50V$ );  
 $(\alpha_2, \alpha_4, \alpha_5)=(-0.5, 0.25, 0.25)$  Pa s;  $\Delta\epsilon_{LF}=+5$ ;  $\Delta\epsilon_{HF}=-4$ ;

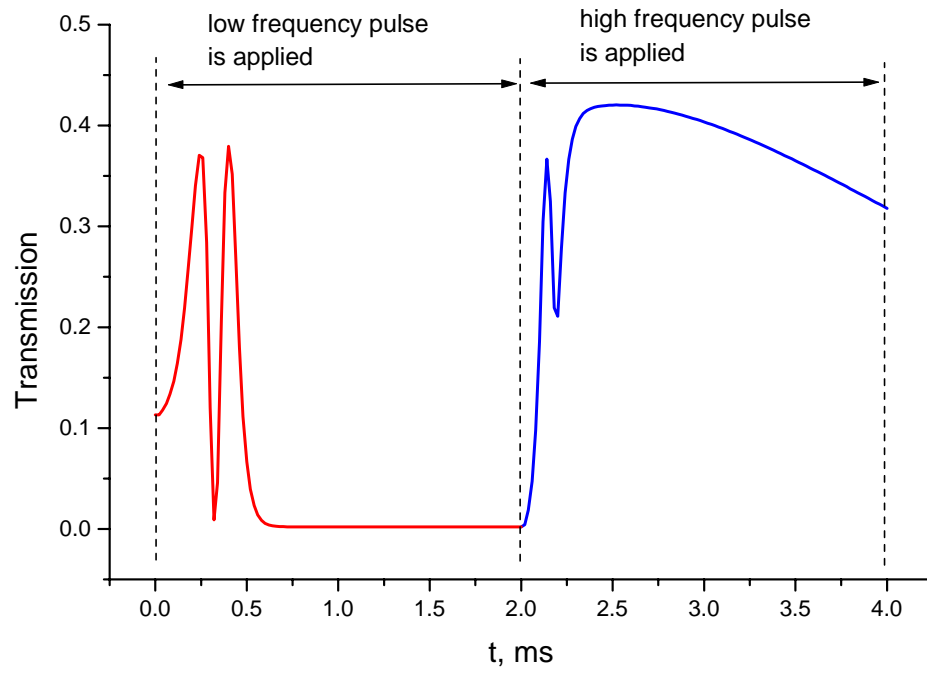


Fig. 8. Dynamics of optical transmission response in case of dual-frequency driving, when the hydrodynamic coupling is taken into account.

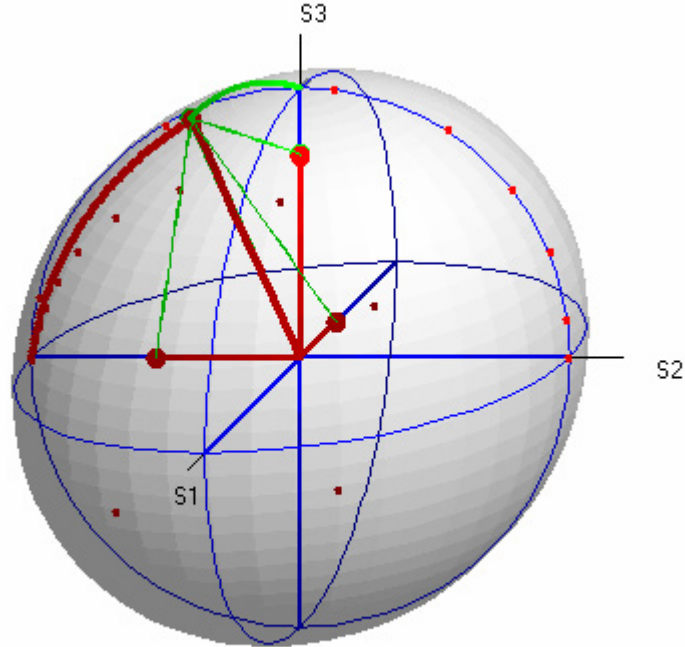


Fig. 9. Light polarization states during high frequency driving ( $t= 2 - 4$  ms in figure 8), when the hydrodynamic coupling is taken into account.



Only at start of the high frequency pulse the polarization state points revolve around  $S_I$  axis by movement along the  $90^\circ$  meridian from point at  $(S_I, S_2, S_3)=(0, 1, 0)$  to the “north” pole  $(S_I, S_2, S_3)=(0, 0, 1)$  and slightly more. Further polarization states become characterizing by non zero value of the  $S_1$  parameter, and they significantly deviate from the  $90^\circ$  meridian. Also no complete turn of the polarization states on the Poincaré sphere exists, and thus, even  $2\pi$ -modulation of the phase retardation is not realized.

The results in Fig. 8 and Fig. 9 are found for  $\alpha_2/\alpha_{4,5}=2$ . We also found that at higher ratios  $\alpha_2/\alpha_{4,5}$  the numerical solution becomes extremely unstable, while decreasing this ratio results in stabilizing the optical transmission response and corresponding revolution of the polarization states, Fig. 10 and Fig. 11. As we see at  $\alpha_2/\alpha_{4,5}=5/3$  optical retardation modulation close to  $2\pi$  is already realized. Moreover, the decreasing high frequency voltage (30V) allows almost  $3\pi$  modulation. All this is well visible on the Poincaré sphere in Fig. 11, where one can see the revolution of the polarization states around the  $S_I$  axis along the curves very close to the  $90^\circ$  meridian.

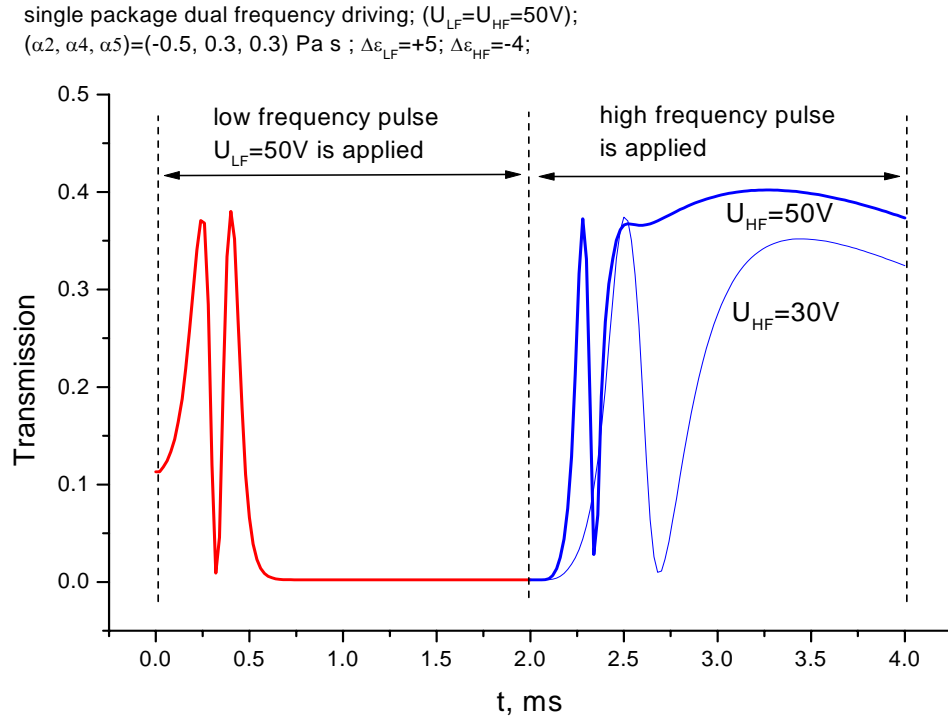


Fig. 10. Dynamics of optical transmission response in case of dual-frequency driving. The hydrodynamic coupling is taken into account. On the interval of high frequency driving the response is shown for two values of the effective voltage.

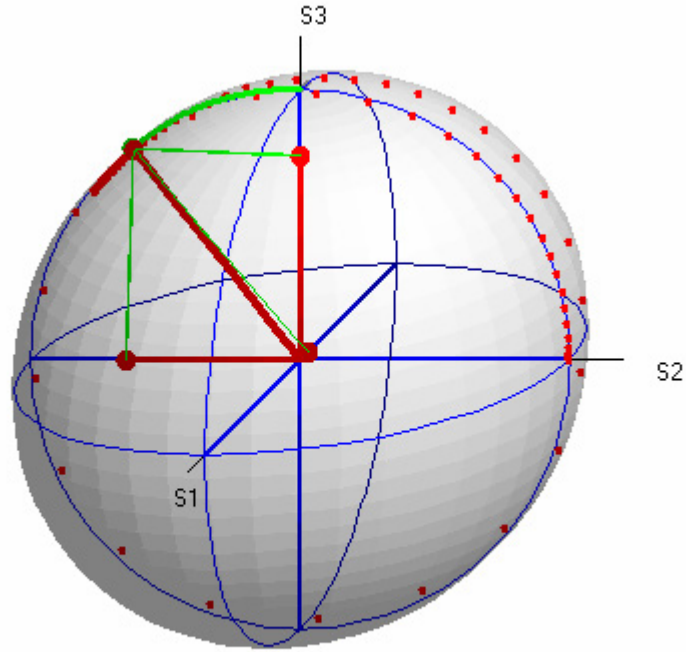


Fig. 11. Light polarization states during high frequency driving  $t = 2 - 4$  ms (see figure 10) at  $U_{HF}=30V$ .

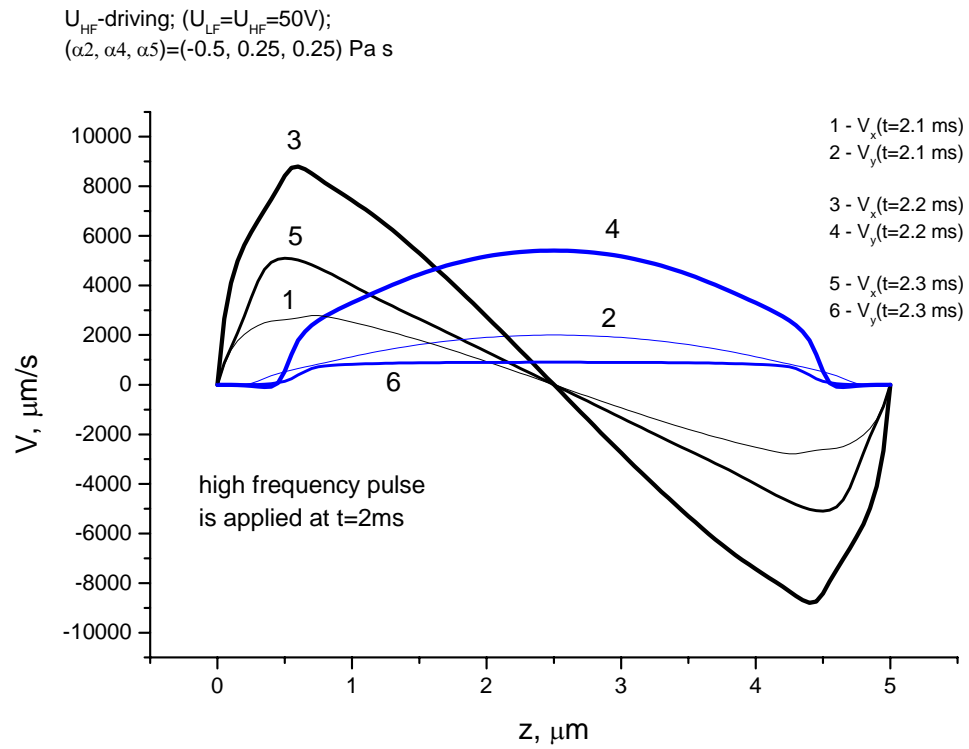


Fig. 12. Hydrodynamic flow velocities (the  $x$ - and  $y$ - components) during high frequency driving  $t = 2 - 4$  ms (see figure 8) at  $U_{HF}=50V$ .

The evolution of the back-flow velocity shown in Fig. 12 allows complete understanding the restrictions for fast phase modulation coming from hydrodynamics. Indeed, in presence of thermal fluctuations or small azimuthal off-set (it can be much less than one degree) of the easy axes orientations at the two boundaries the flow is not more characterized by single  $V_x$  component of the velocity. The  $V_y$  component characterized by very high values ( $\sim 5$  mm/s ) appears. This flow in the  $y$ - direction is the main reason for disturbing the director reorientation making it out of the  $xz$ -plane and providing the phase retardation behavior discussed above.

It is very interesting that there is a small thickness range close to each of the layer boundaries where the  $y$ -component of the flow velocity remains sufficiently low. As one can see from Fig. 12 this thickness range is of about 20% of the total LC layer thickness. Thus for the fast and stable retardation switching namely this thickness range should be used. It allows us to formulate a simple practical rule for an estimation of the optimal LC layer thickness for the fast  $2\pi$ -modulation as:

$$d = \frac{\lambda}{0.2\Delta n} \quad (19A.17)$$

Thus, for example, at  $\Delta n=0.25$  the optimal cell gap for  $\lambda=633\text{nm}$  should be of about  $12.5 \mu\text{m}$ .

## 4. Conclusions

Using numerical simulations we have established the main mechanism providing restrictions for fast retardation switching that is due to by the hydrodynamic destabilization of the plane director field distribution. In particular, using Poincaré sphere presentation we have studied the dynamics of the light polarization states in absence and presence of the hydrodynamic coupling. It is also shown that the hydrodynamic destabilization can be suppressed by increasing the ratio of Leslie coefficients  $|\alpha_2/\alpha_{4,5}|$ . Also we have found that close to the LC layer boundaries there is space region of 20% of the LC layer thickness  $d$ , where the hydrodynamic destabilization is significantly lower compared to the rest region in bulk of the LC cell gap. Thus namely this effective thickness should be used for the fast modulation of the optical retardation.

## References

1. N. G. Basov, P. D. Berezin, L. M. Blinov, I. N. Kompanets, V. N. Morozov, V. V. Nikitin, *Pis'ma v ZhETF*, **15**, № 4, 200 (1972), (in Russian).
2. A. A. Vasil'ev, I. N. Kompanets, A. V. Parfenov, *Sov. J. Quantum Electron.* №13, 689 (1983).
3. A. A. Vasil'ev, A. A. Naumov, V. I. Shmal'gauzen, *Sov. J. Quantum Electron.* №16, 471 (1986).
4. G. Love, *Appl. Opt.* **32**, 2222 (1993).
5. R. Dou, M. K. Giles, *Opt. Lett.* **20**, 1583 (1995).
6. J. A. Baier-Saip, O. Bostanjoglo, H. J. Eichler, R. Macdonald, *J. Appl. Phys.* **78**, 3020 (1995).
7. P. F. McManamon, T. A. Dorschner, D. L. Corcum, L. J. Friedman, D. S. Hobbs, M. Holz, S. Liberman, H. Q. Nguyen, D. P. Resler, R. C. Sharp, E. A. Watson, *Proc. IEEE* **84**, №2, 268 (1996).
8. G. Love, *Appl. Opt.* **36**, 1517 (1997).
9. D. C. Dayton, S. L. Browne, S. P. Sandven, J. D. Gonglewski, A. V. Kudryashov, *Appl. Opt.* **37**, 5579 (1998).
10. T.-L. Kelly, G. D. Love, *Appl. Opt.* **38**, 1986 (1999).
11. M. A. Vorontsov, *J. Opt. Soc. Am. A* **16**, 2567 (1999).
12. T. Martinez, D. V. Wick, S. R. Restaino, *Opt. Express* **8**, 555 (2001).
13. S. R. Restaino, D. Dayton, S. Browne, J. Gomglewski, J. Baker, S. Rogers, S. McDermott, J. Gallegos, M. Shilko, *Opt. Express* **6**, 2 (2000).
14. C.-L. Pan, M. Huang, R.-P. Pan, *Mol. Cryst. Liq. Cryst.* **413**, 561 (2004).
15. H. K. Bucher, R. T. Klingbiel, J. P. Van Meter, *Appl. Phys. Lett.* **25** 186 (1974).
16. E. P. Raynes, J. A. Shanks, *Electr. Lett.* **10**, 114, (1974).

17. W. H. De Jeu, G. J. Gerittsma, P. Van Zanten, W. Y. A. Goossens, Phys. Lett. **39 A**, 355 (1972).
18. G. J. Gerittsma, J.J.M.J. de Klerk, P. Van Zanten, Sol. State Com.**17**, 1077 (1975).
19. C. S. Bak, K. Ko, M.M. Lobes, J. Appl. Phys. **46**, 1 (1975).
20. M. I. Barnik, A. V. Ivashchenko, K. A. Kostilev, B. C. Malofeev, N.M. Shtykov, Opt.-Mechanicheskaya Promishlennost' №5, 25 (1980), (in Russian).
21. S. R. Restaino, D. Dayton, S. Browne, J. Gomglewski, J. Baker, S. Rogers, S. McDermott, J. Gallegos, M. Shilko, Opt. Express **6**, №1, 2 (2000).
22. D. Dayton, S. Browne, J. Gonglewski, S. Resaino, Appl. Opt. **40**, №15, 2345 (2001).
23. A. K. Kirby, G. D. Love, Opt. Express **12**, №7, 1470 (2004).
24. Y.-H. Fan, H. Ren, X. Liang, Y.-H. Lin, S.-T. Wu, Appl. Phys. Lett. **85**, №13, 2451 (2004).
25. Y.-Q. Lu, X. Liang, Y.-H. Wu, F. Du, S.-T. Wu, Appl. Phys. Lett. **85**, №16, 3354 (2004).
26. X. Liang, Y.-Q. Lu, Y.-H. Wu, F. Du, H.-Y. Wang, S.-T. Wu, Jap. J. Appl. Phys. **44**, 1292 (2005).
27. A. B Golovin, S. V. Shiyanovskii, O. D. Lavrentovich, SID 03 DIGEST, 1472 (2003).
28. Y. Yin, M. Gu, A. B. Golovin, S. V. Shiyanovskii, O.D. Lavrentovich, Mol. Cryst. Liq. Cryst. **421**, 133 (2004).
29. Mikhail I. Barnik, Vladimir V. Lazarev, Serguei P. Palto, Serguei V. Yakovlev, in press.
30. M. I. Barnik, V. V. Lazarev, E. E. Maltzev, N. M. Shtykov, Mol. Mat. **6**, 129 (1996).
31. F.M. Leslie, Arch.Ration. Mech.Anal. **28**, 265 (1968).
32. D. W. Berreman, J. Opt. Soc. Am. **62**, 502, (1972).
33. S.P. Palto, JETP **92**, No4, 552 (2001).

## Figure captions

Fig. 1. Electro-optical response measured for the 0-aligned AP-99-1 layers in  $RP_{45}$  and  $RP_0$  geometries at  $U_{LF} = 50V$  and  $T = 22^\circ C$ : a)  $d = 7.6 \mu m$ , curve 1-4 are for  $U_{HF} = 22, 30, 40$  and  $0$  V, respectively; b)  $d = 10 \mu m$ , curve 1-3 are for  $U_{HF} = 30, 38$  and  $51$  V, respectively. The lower trace represents the applied voltage waveform.

Fig. 2. Thickness dependence of high frequency (35 kHz) voltage  $U_{HF}$  at which a dynamic phase retardation change of  $\pi$  (3) and  $2\pi$  (2) is still achieved (100% light modulation efficiency is observed). The curve 1 shows dependence of the threshold voltage of dynamic phase modulation breakdown. The data are for the 0-aligned AP-99-1 layers at  $T = 22^\circ C$ .

Fig. 3. A sketch of the double-layer liquid crystal cell and its connection to the net source. The arrows show the directions of rubbing.

Fig. 4. Electro-optical response of the 0-aligned AP-99-1 layers in a double layer (6.8 and 7.3  $\mu m$ ) cell measured in  $RP_{45}$  and  $RP_0$  geometries at  $U_{LF} = 50V$  ( $T = 22^\circ C$ ): curve 1-4 are for  $U_{HF} = 0, 22, 28$  and  $32$  V, respectively.

Fig. 5. Scheme of simulated electro-optical set-up.

Fig. 6. Dynamics of optical transmission response in case of dual-frequency driving, when the hydrodynamic coupling is neglected

Fig. 7. Light polarization states during high frequency driving ( $t = 2 - 4$  ms in Fig. 6), when hydrodynamic coupling is neglected

Fig. 8. Dynamics of optical transmission response in case of dual-frequency driving, when the hydrodynamic coupling is taken into account.

Fig. 9. Light polarization states during high frequency driving ( $t = 2 - 4$  ms in figure 8), when the hydrodynamic coupling is taken into account.

Fig. 10. Dynamics of optical transmission response in case of dual-frequency driving. The hydrodynamic coupling is taken into account. On the interval of high frequency driving the response is shown for two values of the effective voltage.

Fig. 11. Light polarization states during high frequency driving  $t = 2 - 4$  ms (see figure 10) at  $U_{HF} = 30V$ .

Fig. 12. Hydrodynamic flow velocities (the  $x$ - and  $y$ - components) during high frequency driving  $t = 2 - 4$  ms (see figure 8) at  $U_{HF} = 50V$ .